Structural, Magnetic and Magnetotransport Properties of $La_{0.7}Ca_{0.18}Ba_{0.12}Mn_{0.95}Sn_{0.05}O_3$ Perovskite Manganite

I. Belal[a,*], F. Meriche[a], N. Mahamdioua[b], J.A. Alonso[c], J.L. Martinez[c], S. Polat-Altintas[d] and C. Terzioglu[d]

[a] *LEM laboratory, Department of Physics, University of Jijel, Jijel 18000, Algeria*
[b] *LEND Laboratory, Faculty of Science and Technology, University of Jijel, Jijel 18000, Algeria*
[c] *Instituto de Ciencia de Materiales de Madrid, CSIC, Cantoblanco, 28049 Madrid, Spain*
[d] *Department of Physics, Faculty of Arts and Sciences, AIB University, Bolu 14280, Turkey*

Received: 25.08.2025 & Accepted: 19.01.2026

Doi: 10.12693/APhysPolA.149.65 *e-mail: ibtihalbelal94@gmail.com

This paper reports a study on the structural, magnetic and magnetotransport properties of the mixed-valence perovskite manganite $La_{0.7}Ca_{0.18}Ba_{0.12}Mn_{0.95}Sn_{0.05}O_3$ (LCBMSO), synthesized by a solid-state reaction method. The results of X-ray powder diffraction analysis confirm that the sample possesses a single orthorhombic phase with space group *Pnma*. The Rietveld refinement results reveals that LCBMSO contains distorted MnO_6 octahedron. Micrographs obtained by scanning electron microscopy showed that the sample grains have a polygonal shape and are in the micrometer size range. Fourier transform infrared spectroscopy analysis confirms the presence of Mn–O–Mn and Mn–O stretching vibration. The magnetization–temperature curve displays a paramagnetic–ferromagnetic transition at $T_C = 145$ K. A slight bifurcation between the zero-field curve and the cooling-field curve was noticed, which is attributed to spin-glass behavior. Based on the hysteresis cycle, a soft ferromagnetic behavior was observed in our sample at temperatures of 1.8 and 100 K. The electrical resistivity vs temperature curve shows a metal–insulator transition at $T_{MI} = 154$ K. The magnetoresistance ratio reached 30% at an applied magnetic field of 1 T, making the LCBMSO material an attractive candidate for use as a magnetoresistive sensor in various industrial applications. The temperature coefficient of resistivity reached 3.35%, making this material suitable for use in infrared and bolometric detectors. The relation $\rho = \rho_0 - \rho_{0.5}T^{0.5} + \rho_2 T^2 + \rho_5 T^5$ was employed to fit the low-temperature resistivity data below T_{MI}, whereas the variable range hopping and small polaron hopping models were used to fit the data in the insulating region above T_{MI}.

topics: manganites, magnetic properties, magnetotransport properties, temperature coefficient of resistivity

1. Introduction

Manganese oxide perovskites $Ln_{1-x}A_xMnO_3$, where Ln represents trivalent rare earth elements (La^{3+}, Sm^{3+}, etc.) and A represents divalent alkaline earth metals (Ca^{2+}, Sr^{2+}, etc), have intrigued the scientific community due to their unique physical properties, such as colossal magnetoresistance (CMR) [1], charge and/or orbital ordering, and magnetocaloric effect (MCE) [2]. These materials are highly valuable for various applications such as magnetic data storage, infrared bolometry, and magnetic refrigeration [3–5]. Oxides such as $LaMnO_3$ are typical examples of simple perovskites. The electrical transport and magnetic properties of these materials can be modified by changing the sintering conditions and substituting different elements at the La and Mn sites [6]. The parent compound $LaMnO_3$ has an A-type antiferromagnetic (AFM) character, which is related to the super-exchange (SE) interaction between the Mn^{3+} sites. Divalent substitution (Ba^{2+}, Ca^{2+}, Sr^{2+},...) at the Ln site produces Mn^{4+} ions with the electronic configuration ($3d^3$; $t_{2g}^3 \uparrow e_g^0$; $S = 3/2$). Accordingly, the e_g electrons are supposed to be delocalized — this facilitates transfer of charge in the e_g band and mediates ferromagnetic (FM) coupling between Mn ions via the double-exchange (DE) mechanism. The coupling leads to DE interaction [7]. Furthermore, such doping affects the average A-site radius, its cation mismatch σ^2 [8, 9], Jahn–Teller distortion (JT), and Mn^{3+}/Mn^{4+} ratio [10]. Substitution of divalent ions like Ca^{2+}, Ba^{2+}, Sr^{2+}

into $LaMnO_3$ creates a mixed valence state of manganese (Mn^{3+} and Mn^{4+}), which profoundly influences physical properties of this state. This phenomenon can be studied by referring to the structural and magnetic phase diagrams developed for the $La_{1-x}Ca_xMnO_3$ and $La_{1-x}Sr_xMnO_3$ systems [3, 11]. $La_{1-x}Ca_xMnO_3$ (LCMO) compounds have garnered significant interest due to their large magnetoresistance (MR) and magnetocaloric effect (MCE), making them promising candidates for diverse applications [12–15].

A key challenge associated with the LCMO compounds is that their Curie temperatures T_C are well below room temperature. Alternatively, the effect of doping at the Ca site with larger cations, including Ba, Pb and Sr, has been explored in various studies [16–18]. Barium-doped manganites, such as $La_{0.65}Ca_{0.35-x}Ba_xMnO_3$, are of particular interest due to the very large difference in ionic sizes between Ca and Ba, which leads to the observed increase in the Curie temperature T_C with increasing Ba content [19–21]. According to the literature, dopants with larger ionic radii have a high impact on the mismatch factor σ^2 [22, 23].

Although magnetoresistance (MR) is generally one of the most extensively studied properties in manganite systems, relatively few studies have focused specifically on the MR behavior in Ba-doped LCMO compounds, particularly in combination with B-site co-doping, such as Sn [24]. On the other hand, substitution of divalent, trivalent, or tetravalent elements at the Mn site modifies the Mn^{3+}/Mn^{4+} ratio, which can significantly influence the crystal structure as well as the magnetic and magnetotransport properties of manganese oxides [25]. Song et al. [26] reported the effect of replacing Mn with X = Fe, Co, Ni on the electrical and magnetic properties of manganites. They deduced that doping decreased both the metal–insulator (M–I) transition temperature and the saturation magnetization, while increasing the electrical resistivity of the samples. Likewise, Qin et al. [25] found that substituting Mn with Al^{3+} enhanced the magnetoresistance of the $La_{0.67}Sr_{0.33}Mn_{1-x}Al_xO_3$ system.

According to the literature, Sn substitution at the Mn site influences the physical properties of manganites [27, 28]. Li et al. [28] investigated the effect of Sn^{4+} ions incorporation on the magnetic and magnetotransport properties. They found that the Curie temperature (T_C) decreases at low doping levels in manganites $La_{0.5}Ca_{0.5}Mn_{1-x}Sn_xO_3$ ($0 \leq x \leq 0.06$). They deduced that the introduction of Sn destroys the charge-ordered state. E. Tka et al. [29] studied the impact of Sn substitution on the evolution of structural, magnetic and magnetocaloric properties in $La_{0.57}Nd_{0.1}Sr_{0.33}Mn_{1-x}Sn_xO_3$ ($0.05 \leq x \leq 0.3$). They reported that the addition of tin leads to a decrease in magnetization, a reduction in the Curie temperature, and an increase in the entropy.

Among all the properties, magnetoresistance (MR) stands out as the most extensively studied. It involves the variation in electrical resistivity when an external magnetic field is applied, and it serves as a crucial factor in evaluating the performance of magnetic sensors [30]. In fact, the application of an external magnetic field has a significant impact on the physical properties of manganite-based materials. Namely, it decreases the electrical resistivity around the M–I transition temperature and enhances both the MR and the temperature coefficient of resistivity (TCR), which is an essential factor in describing the sharpness of the M–I transition [31].

In this study, we selected the composition $La_{0.7}Ca_{0.18}Ba_{0.12}Mn_{0.95}Sn_{0.05}O_3$ to investigate the combined effect of substitutions at both the A-site (Ba^{2+}) and the B-site (Sn^{4+}) in an LCMO-based matrix. The motivation behind this specific composition stems from prior studies showing that Ba^{2+} substitution increases the average A-site ionic radius, thereby enhancing the Curie temperature T_C by improving the double-exchange interaction. Simultaneously, Sn^{4+} substitution at the B-site is known to influence electron localization and suppress charge ordering, even at low doping concentrations. The selected doping levels were carefully chosen to achieve measurable changes in material properties while maintaining phase purity and avoiding the formation of secondary phases.

Unlike our previous report on the same composition $La_{0.7}Ca_{0.18}Ba_{0.12}Mn_{0.95}Sn_{0.05}O_3$, which primarily focused on the structural and transport properties, the present study provides a comprehensive magnetic investigation, enabling a deeper understanding of the structure–magnetism–transport correlation in this system. Accordingly, this work aims to systematically investigate the structural, magnetic, electrical, and magnetotransport properties of $La_{0.7}Ca_{0.18}Ba_{0.12}Mn_{0.95}Sn_{0.05}O_3$ manganite (referred to as LCBMSO through this paper).

2. Experiment details

Polycrystalline sample with the composition LCBMSO was prepared by the solid-state reaction method using stoichiometric proportions of La_2O_3, $CaCO_3$, $BaCO_3$, MnO_2 and SnO_2 as precursors. The mixture was calcinated at 900°C for 14 h, and then pressed into pellets under pressure of 4 tons and sintered at rates of 1150°C/10 h, 1160°C/10 h with intermediate regrinding and pressing. Finally, the sample was sintered at 1170°C/10 h and cooled down in a furnace. Powder X-ray diffraction (XRD) technique was employed to examine the structure and phase purity of the sample using a Bruker AXS D8-Advance X-ray diffractometer with monochromatic Cu K_α radiation ($\lambda = 1.54051$ Å). The XRD pattern was obtained in the range $20° \leq 2\theta \leq 80°$

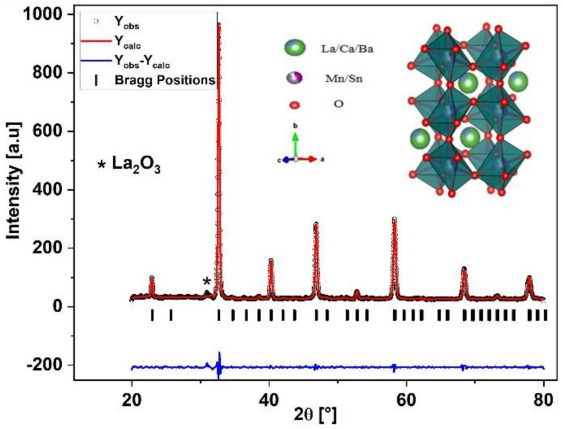

Fig. 1. XRD pattern of the compound $La_{0.7}Ca_{0.18}Ba_{0.12}Mn_{0.95}Sn_{0.05}O_3$. The inset depicts the crystal structure.

TABLE I

Lattice parameters and refinement factors of LCBMSO.

Parameter	Unit	Value
Space group		P*nma*
Lattice parameters		
a	[Å]	5.486(2)
b	[Å]	7.756(1)
c	[Å]	5.481(2)
V	[Å^3]	233.22(1)
La_2O_3	[%]	8.40
Discrepancy factors		
R_p	[%]	14.1
R_{wp}	[%]	11.7
GOF		0.36

with a step size of 0.016°. The FULLPROF program, which is based on the Rietveld method, was used to perform the Rietveld refinement analysis of XRD data [32]. A scanning electron microscopy (SEM) using JEOL 6390-LV was utilized to examine the sample's microstructure, while the energy dispersive X-ray (EDAX) was employed to check its elemental composition and purity. The infrared (IR) transmission spectrum was measured by IRAffinity-1S SHIMADZU FTIR spectrophotometer. The magnetization of the sample was measured using a SQUID magnetometer (MPMS-3 from Quantum Design, San Diego, USA) in the range of 1.6–400 K under magnetic field up to 7 T. Electrical resistivity measurements were performed between 5 and 300 K under 0 and 1 T magnetic fields by using the standard four-probe method with a He-gas contact cryocooler and a superconducting magnet system (Cryo Industries, USA).

3. Results and discussion

3.1. XRD analysis

The XRD pattern of the prepared sample LCBMSO taken at room temperature is shown in Fig.1. According to the Rietveld refinement of the XRD data using FULLPROF software [33], a single-phase orthorhombic crystal structure was identified for the LCBMSO sample (SG P*nma*) with an impurity phase (unreacted La_2O_3 oxide) [34]. The inset in Fig. 1 shows a three-dimensional visualization of the crystal structure and the MnO_6 octahedron established by software VESTA (Visualization for Electronic and Structural Analysis) using refined lattice parameters, space group and atomic positions [35]. The refined cell parameters and unit cell volume are summarized in Table I; the refinement factors (R_{wp}, R_p and goodness of fit (GOF)) are also given. The atomic positions, bond distances and bond angles, are listed in Table II. The goodness of fit is ≈ 0.36, proving the quality of the fit.

Based on the average Mn–O distances and the average Mn–O–Mn angles, it is assumed that the MnO_6 octahedron undergoes a distortion, which is quantified by the Goldschmidt tolerance factor [36]

$$t_{exp} = \frac{d_{\text{A-O}}}{\sqrt{2}\, d_{\text{B-O}}}, \tag{1}$$

where $d_{\text{A-O}}$ and $d_{\text{B-O}}$ are average bond-lengths between A–O and B–O, respectively (see Table II). For detailed values of this factor, please consult [24]. In the present work, t_{exp} was found to be 0.8857, which corresponds to an orthorhombic structure.

It is noticeable that the lattice parameters satisfy the relation $a \geq b/\sqrt{2} \geq c$; this signifies that the sample may have an O-type lattice distortion, probably originated from the Jahn–Teller effect [37], leading to distorted MnO_6 octahedra. In this respect, the Jahn–Teller distortion is expressed as follow [38]

$$\delta_{\text{JT}} = \sqrt{\frac{1}{3}\sum_{i=1}^{3}\left[(\text{M–O})_i - \langle \text{M–O} \rangle\right]^2}, \tag{2}$$

where (Mn–O) denotes the different bond distance and $\langle$M–O$\rangle$ is the average bond distance. The δ_{JT} value was found to be 0.0825 (Table III), which is nearly equal to the values reported for other orthorhombic manganites [39]. As a result, a decrease in t_{exp} compared to the ideal cubic structure ($t = 1$) causes a release of strain for LCBMSO and an increase in orthorhombic distortion D (see Table III). The distortion D was calculated using the following relation [40]

$$D = \frac{1}{3}\sum_{i=1}^{3}\left|\frac{a_i - \bar{a}}{a_i}\right|, \tag{3}$$

where $\bar{a} = (a_1\, a_2\, a_2)^{1/3}$, and $a_1 = a$, $a_2 = b/\sqrt{2}$, $a_3 = c$.

TABLE II

Refined structural parameters obtained from the X-ray Rietveld refinement for LCBMSO.

Parameter	Value
Atomic position (La/Ca/Ba)	
x	0.01210
y	0.25000
z	−0.0042
O_{cc}(La)	0.69253
O_{cc}(Ca)	0.17995
O_{cc}(Ba)	0.11968
Atomic position (Mn/Sn)	
x	0.00000
y	0.00000
z	0.50000
O_{cc}(Mn)	0.89000
O_{cc}(Sn)	0.51000
Atomic position O(1)	
x	0.27028
y	0.08940
z	1.25018
O_{cc}	1.73753
Atomic position O(2)	
x	0.48993
y	0.25000
z	0.00737
O_{cc}	2.14941
Bond distance [Å]	
$d_{\text{A-O}}$	2.5309
$d_{\text{B-O}}$	2.0205
Bond angles [°]	
⟨Mn/Sn–O–Mn/Sn⟩	158.1561

Based on the main Bragg reflection peak in the diffraction pattern, the average crystallite size was estimated using the Scherer's expression [41]

$$D_{sc} = \frac{K\lambda}{\beta_{hkl}\cos(\theta)}, \tag{4}$$

where D_{sc} is the crystallites size, $\lambda = 1.5406$ Å is the X-ray wavelength of Cu K_α radiation, K is the shape factor equal to 0.9, and β_{hkl} is the full width at half maximum (FWHM) of the highest peak. The value of D_{sc} is found to be 28.66 nm, as presented in Table III. The dislocation density (δ) represents an estimate of the dislocation line length per unit crystal volume. It is calculated using the following expression [42]

$$\delta = \frac{1}{D_{sc}^2}, \tag{5}$$

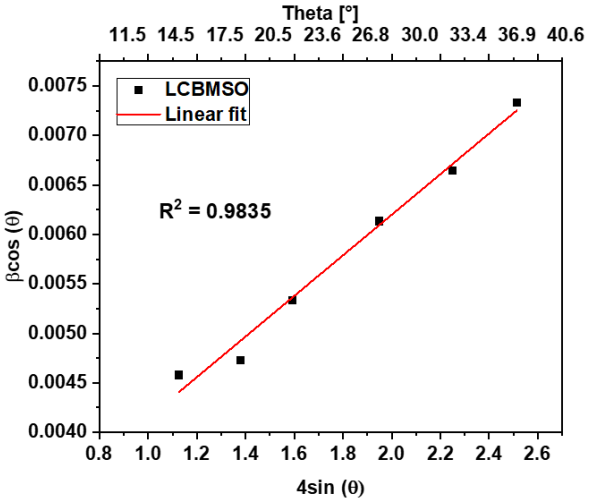

Fig. 2. Williamson–Hall plot for the LCBMSO sample.

TABLE III

Structural parameters obtained from XRD analysis for LCBMSO.

Parameter	Unit	Value
D_{sc}	[nm]	28.66
D_{WH}	[nm]	64.50
δ	[nm^{-2}]	0.0012
ε ($\times 10^{-2}$)		0.2100
t_{exp}		0.8857
Orthorhombic distortion (d_{ortho})		0.4832
W	[eV]	0.0837
δ_{JT}		0.0825

where D_{sc} is the crystallite size. The obtained value is listed in Table III. Since δ represents the number of defects in the sample, the small δ value obtained in this study confirmed the high crystallinity of our sample [43].

Moreover, the Williamson–Hall method (W–H) [44] was used to assess the peak broadening associated with crystallite size and microstrains arising from crystal defects and distortion. The W–H method can be expressed as follow

$$\beta\cos(\theta) = \frac{K\lambda}{D_{\text{WH}}} + 4\,\varepsilon\,\sin(\theta). \tag{6}$$

The average crystallite D_{WH} and lattice strain ε were calculated from the intercept and slope of the $\beta\cos(\theta)$ versus $4\,\varepsilon\sin(\theta)$ plot (Fig. 2). The estimated values of crystallite size and strain of the LCBMSO compound obtained by the Scherer and Williamson–Hall methods are summarized in Table III. Based on these results, we can deduce that the D_{WH} value is significantly greater than the value of D_{sc}, because the strain broadening effect is taken into account in the W–H method [45].

3.2. Scanning electron microscopy analysis

The morphological structure of our sample was investigated using scanning electron microscopy (SEM). The micrograph of the LCBMSO grain size and its corresponding histogram are shown in Fig. 3. The SEM image depicts a granular surface structure with grains of various sizes and shapes. In the polygonal grain matrix, needle-like substances appeared. ImageJ software [46] was used to calculate the average grain size without taking needle-like grains into consideration. The grain size ranges from 0.5 to 8 μm, which is lower than that obtained by Boufligha et al. [47]. This difference can be attributed to the last sintering temperature chosen when preparing each sample.

The EDAX spectrum observed in Fig. 4 depicts the presence of the elements La, Ca, Ba, Mn, and Sn, which proves that no constituent element is completely lost during during the solid-state preparation of the LCBMSO compound. The presence of a carbon peak could result from the sample environment, the specimen holder, the analysis chamber itself, or from surface contamination introduced by the adhesive tape used during the EDAX analysis. On the other hand, the presence of silicate oxides causes the appearance of the Si peak in the EDAX spectrum [48], which we believe is caused by the processing conditions, such as contamination from the crucible or furnace environment, or interactions with silicon-containing materials during calcination or sintering, which can lead to the unintentional incorporation of Si into the sample. The presence of silicate oxides in the matrix is undoubtedly related to the formation of needle-like grains.

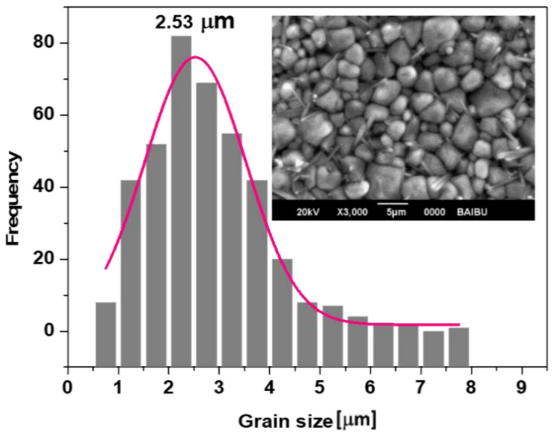

Fig. 3. Histogram showing average grain sizes. The inset represents a scanning electron micrograph of the LCBMSO compound.

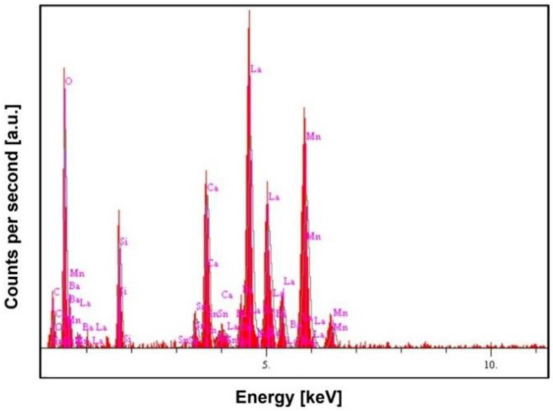

Fig. 4. EDX spectrum of LCBMSO compound.

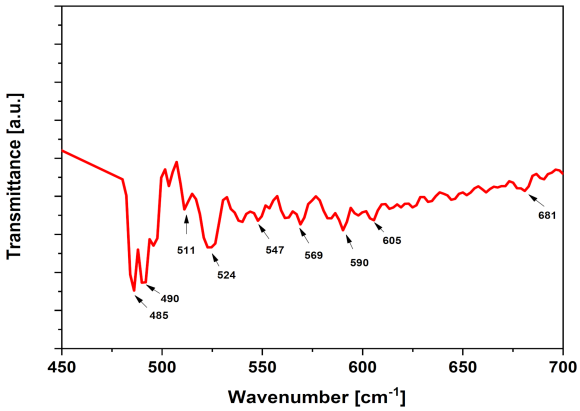

Fig. 5. Infrared transmittance spectrum of LCBMSO taken in the frequency range 450–700 cm^{-1}.

3.3. FTIR analysis

The Fourier transform infrared spectroscopy (FTIR) spectrum presented in Fig. 5 was recorded in the range of 450–700 cm^{-1}. The presence of vibrational bands in the 450–700 cm^{-1} range confirms the formation of the ABO_3 perovskite structure for our LCBMSO compound [49]. The vibrational bands observed at 485 and 490 cm^{-1} are attributed to the Mn/Sn–O–Mn/Sn bond bending mode of the $(Mn/Sn)O_6$ octahedron [50]; whereas, the vibrational bands ranging from 511 to 681 cm^{-1} correspond to the stretching mode of the Mn/Sn–O bond, which can be related to the Jahn–Teller effect [51]. The appearance of these vibrating modes supports the formation of $La_{0.7}Ca_{0.18}Ba_{0.12}Mn_{0.95}Sn_{0.05}O_3$ simple perovskite manganite, which is consistent with the X-ray diffraction results.

The transmission wavenumber (ν) of the stretching vibration of the Mn/Sn–O bond can be determined using Hook's law [52]

$$\nu = \frac{1}{2\pi c}\left(\frac{k}{\mu}\right)^{1/2}, \tag{7}$$

TABLE IV

Values of the wavenumber, effective masse, force constant and Mn/Sn–O bond distance for the $La_{0.7}Ca_{0.18}Ba_{0.12}Mn_{0.95}Sn_{0.05}O_3$ compound.

FTIR results		
Parameter	Unit	Value
Wavenumber	[cm^{-1}]	524
Effective mass ($\times 10^{-26}$)	[kg]	2.083
Force constant k	[N/cm]	2.693
Bond distance of Mn/Sn–O obtained from FTIR	[Å]	1.848
Bond distance of Mn/Sn–O obtained from Rietveld	[Å]	2.020

where ν is the wavenumber, k is the force constant of the (Mn/Sn–O–Mn/Sn) bond, c is the velocity of light, and μ is the effective masse of the Mn/Sn–O bond, determined by the following relation

$$\mu = \frac{M_O\, M_B}{M_O + M_B}. \tag{8}$$

In (8), M_O is the atomic weight of oxygen, and M_B is the atomic weight of the B-site elements. In our case, the B site is occupied by two elements (Mn and Sn), and M_B is expressed by the formula

$$M_B = 0.95 M_{Mn} + 0.05 M_{Sn}, \tag{9}$$

where M_{Mn} and M_{Sn} are the atomic masses of Mn and Sn, respectively.

The force constant can be related to the average Mn/Sn–O bond distance (r) using the expression [53]

$$k = \frac{17}{r^3}. \tag{10}$$

Using (7)–(10), the Mn/Sn–O bond distance, effective mass, and force constant were calculated from the FTIR spectrum and the results are collected in Table IV. It is worth noting that the Mn/Sn–O bond calculated from the FTIR spectrum is in accordance with the results obtained from the Rietveld refinement.

3.4. Magnetic measurements

To study the magnetic properties of the LCBMSO compound, we measured the magnetization vs temperature in two modes (Fig. 6a), namely zero-field-cooled (ZFC) mode and field-cooled (FC) mode, recorded in the temperature range 1.6–400 K under an applied magnetic field of 100 Oe. The results of this measurement demonstrate that in the ZFC mode, the magnetization increases to a maximum at $T \simeq 116$ K, and then gradually decreases up to 400 K. In the FC mode, the magnetization curve shows a clear bifurcation from the ZFC curve

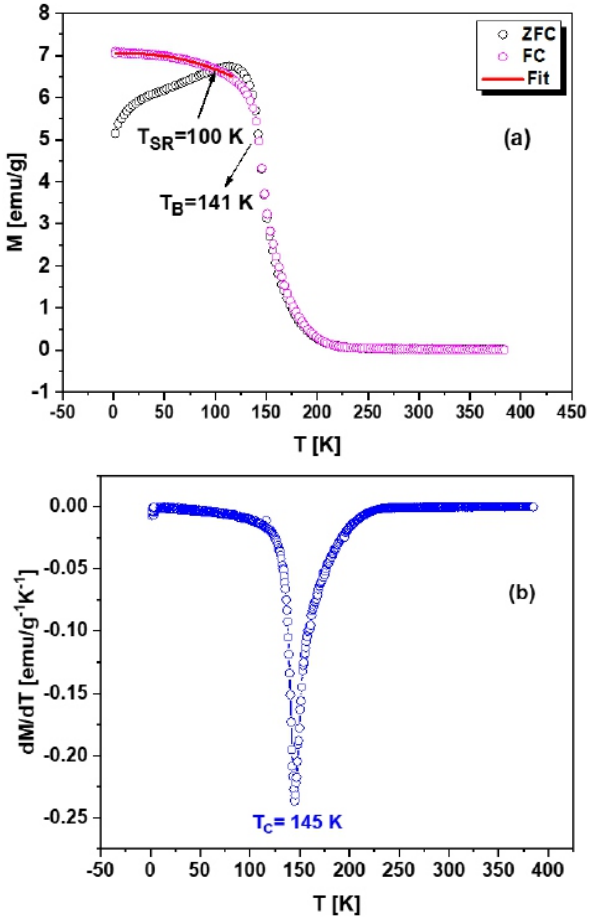

Fig. 6. (a) Temperature dependence of magnetization measured at a magnetic field of $\mu_0 H = 100$ Oe, and (b) the derivative dM/dT versus temparature.

at $T \simeq 141$ K — this could be due to spin reorientation or a spin glass behaviour of the sample [37]. The FC magnetization decreases and intersects the ZFC curve at $T_{SR} = 100$ K, corresponding to the spin reversal temperature. The Curie temperature T_C value was fixed at the minimum of dM/dT and found to be 145 K for the LCBMSO compound (Fig. 6b). This value is lower than that reported in the previous study for the undoped compound $La_{0.7}Ca_{0.18}Ba_{0.12}MnO_3$ [54]. This difference could be attributed to the substitution of Mn by a non-magnetic element Sn with an electronic configuration $4d^{10}$, causing a break of the ferromagnetic interactions Mn^{3+}–O–Mn^{4+} — possible reason of the decrease in T_C [47].

As widely established, the magnetic and magnetotransport properties are governed by the one-electron bandwidth W, as described by

$$W = \frac{\cos\left(\frac{1}{2}\left(\pi - \langle \text{Mn/Sn–O–Mn/Sn} \rangle\right)\right)}{\sqrt{d^3_{\text{Mn/Sn–O}}}}, \tag{11}$$

where Mn/Sn–O–Mn/Sn is the average bond angle and $d_{\text{Mn/Sn–O}}$ is the average bond distance.

TABLE V

Summary of magnetic data for $La_{0.7}Ca_{0.18}Ba_{0.12}Mn_{0.95}Sn_{0.05}O_3$ compound.

Parameter	Unit	Value
T_C	[K]	145
θ_{cw}	[K]	197.3
C	$\left[\frac{\text{emu K}}{\text{Oe mol}}\right]$	5.622
μ_{eff}^{exp}	[μ_B]	6.700
μ_{eff}^{theo}	[μ_B]	4.533

The substitution of tin for manganese changes structural parameters, such as the Mn–O bond distance and the Mn–O–Mn bond angle, leading to a reduction in the charge carrier bandwidth W, calculated to be 0.0837 eV (Table III). This decrease in W reduces the overlap between Mn $3d$ and O $2p$ orbitals, which in turn diminishes the Mn^{3+}–O–Mn^{4+} exchange coupling and lowers T_C [55]. For a better understanding of the magnetic behavior in the ferromagnetic phase, the dependence of FC magnetization vs temperature was investigated by using spin wave theory. Usually, in manganite systems, spin waves, their fluctuations and domain boundaries play a key role in influencing ferromagnetism [56]. In this sense, Lonzarich and Taillefer [57] proposed that spin wave theory can explain how magnetization works in manganite compounds. Magnetization changes as $T^{3/2}$ (Bloch's law) at low temperature, and as T^2 across a large temperature range. However, at temperatures close to T_C, magnetization changes as $\sqrt{1-(T/T_C)^{4/3}}$.

In view of this, in the ferromagnetic region, the magnetization data were fitted using the following equation

$$M(T) = M_0 + M_{3/2}\,T^{3/2} + M_2\,T^2, \tag{12}$$

where M_0 represents the temperature-independent spontaneous magnetization. Figure 6 shows the best fit curve. It can be concluded that the FM behavior of the LCBMSO compound can be well-described within the framework of spin-wave theory [58].

In order to investigate the magnetic interaction in the paramagnetic region ($T > T_C$), we determine the inverse of the susceptibility (χ^{-1}) versus temperature (T), as shown in Fig. 7. In this region, the susceptibility follows the Curie–Weiss law

$$\chi = \frac{C}{T-\theta_{cw}}, \tag{13}$$

where θ_{cw} represents the Curie–Weiss temperature and C refers to the Curie constant, defined as

$$C = \frac{N_A \mu_B^2}{3k_B}\left(\mu_{eff}^{exp}\right)^2. \tag{14}$$

Here, $N_A = 6.023\times10^{23}$ mol^{-1} is the Avogadro number, $\mu_B = 9.274\times10^{-24}$ J/T is the Bohr magneton, and $k_B = 1.38016\times10^{-16}$ erg/K is the Boltzmann constant. The experimental effective magnetic moment μ_{eff}^{exp} of the LCBMSO compound in the paramagnetic (PM) region was determined by the following expression [55]

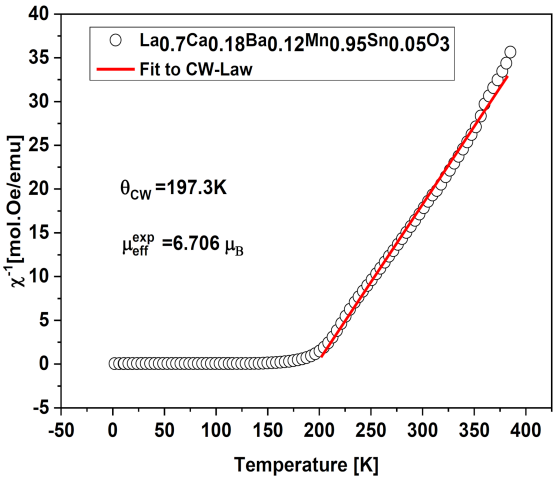

Fig. 7. Thermal dependence of inverse susceptibility ($\chi^{-1} = H/M$) of LCBMSO compound.

$$\mu_{eff}^{exp} = 2.828\sqrt{C}\,\mu_B, \tag{15}$$

where C is the slope of the linear curve (χ^{-1} vs T). For Mn^{3+} or Mn^{4+}, the orbital moment is quenched ($L = 0$), and as a result S is the accurate quantum number. We can write

$$\mu_{eff}(S) = g\,\mu_B\sqrt{S(S+1)}, \tag{16}$$

where $g = 2$ is the Landé factor. We assume $S = 2$ for Mn^{3+} and $S = 3/2$ for Mn^{4+}, which leads to $\mu_{eff}(Mn^{3+}) = 4.9\mu_B$ and $\mu_{eff}(Mn^{4+}) = 3.87\mu_B$ [59]. The theoretical effective magnetic moment μ_{eff}^{theo} is described by the following equation

$$\mu_{eff}^{theo} = \sqrt{0.7\,\mu_{Mn^{3+}}^2 + (0.3-0.05)\,\mu_{Mn^{4+}}^2}\ . \tag{17}$$

From the linear fit of the PM region to the Curie–Weiss law, the parameters C and θ_{cw} were determined. The positive value of θ_{cw}, equal to 197.3 K (Table V), implies the ferromagnetic interaction between spins in the LCBMSO compound, supporting its classification as a ferromagnetic material [34]. The extracted value is higher than the T_C value due to the existence of a short-range FM interaction [60]. The obtained values of μ_{eff}^{exp} and μ_{eff}^{theo} are summarized in Table V. In addition, the observed difference between the experimental and the theoretical effective magnetic moments might be due to short-range ferromagnetic interactions in the material [61].

Figure 8a shows the field-dependent magnetization $M(H)$ for the LCBMSO sample. The M–H data has been gathered at various temperatures: 1.8, 100, and 300 K, in the magnetic field range of $H = \pm50$ kOe. From this figure, we observe that the LCBMSO sample exhibits a similar hysteresis

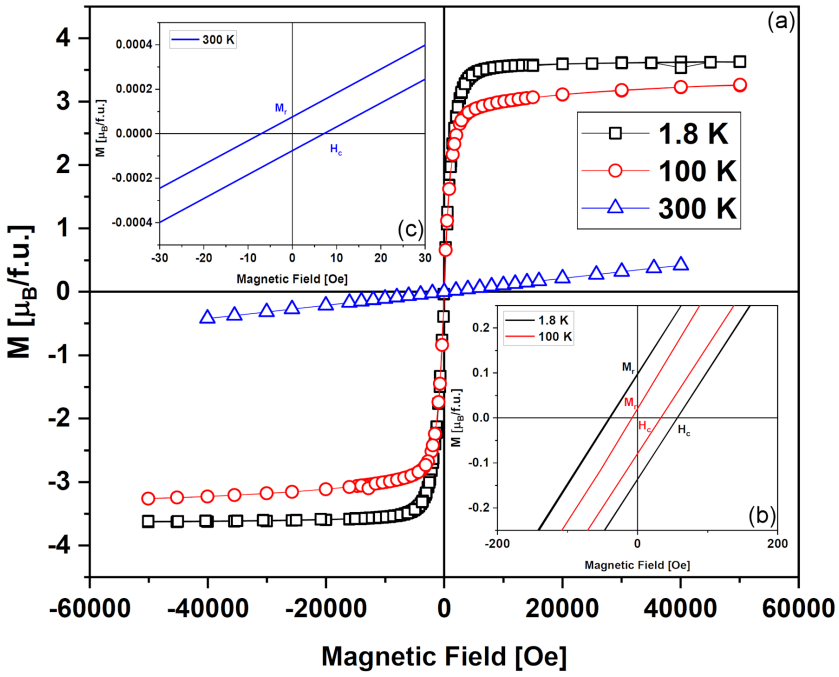

Fig. 8. (a) Hysteresis curves of the LCBMSO compound, measured at different temperatures T = 1.8, 100, 300 K. Insets (b, c) show zoom of the hysteresis curves.

loop at 1.8 and 100 K. Notably, the magnetization increases sharply at low magnetic field. We noticed significant saturation, with M_s values of 88.53 emu/g at 1.8 K and 79.98 emu/g at 100 K; this is evidence of FM behavior of the sample. Moreover, Fig. 8b shows a magnified view of the low magnetic field part; we noticed that LCBMSO has low coercive fields (H_c) and remanent magnetization (M_r) at 1.8 and 100 K (see Table VI). From these values, we can deduct that our sample exhibits soft FM behavior. This makes it suitable for the fabrication of high-density data storage devices [62]. Nevertheless, we have observed no saturation at 300 K. Figure 8c shows that the sample exhibits lower remanent magnetization; this indicates that at 300 K the LCBMSO compound is paramagnetic.

TABLE VI

Values of saturation magnetization (M_s), remanent magnetization (M_r) and coercive field (H_c) for LCBMSO at different temperatures.

Sample	M_s [μ_B/f.u.]	M_r [μ_B/f.u.]	H_c [Oe]
1.8 K	3.60	0.1	57.2
100 K	3.25	0.02	33.7
300 K	–	0.001	7.3

3.5. Electrical properties

Figure 9 depicts the temperature dependence of the resistivity measured in a magnetic field of 0 and 1 T, and the magnetoresistance (MR) as a function of temperature for the LCBMSO sample. Due to ferromagnetic coupling, LCBMSO is magnetically ordered, its resistivity at low temperatures displays a metallic behavior below T_{MI}, the temperature at which resistivity reaches its maximum value. At high temperatures, the sample exhibits a semiconductor behavior above T_{MI}. The metal–insulator transition temperature (T_{MI}) is observed around 154 K for the sample without an applied magnetic field, while it rises up to about 4 K toward high temperatures in a 1 T magnetic field. It is noticeable that the magnitude of the resistivity in the presence of a 1 T magnetic field is lower compared to the resistivity value without an applied magnetic field.

Actually, applying an external magnetic field reduces electron scattering at grain boundaries, causes magnetic moments to be reoriented toward the applied field, and decreases the magnetic disorder. As a result, the PM insulating regime can be partially suppressed in favor of the FM metallic state, leading to the increase in T_{MI}. This aligns with the double-exchange (DE) model [63]. Compared with previous results [47], the present one shows larger resistivity values and a lower metal–insulator transition temperature. This difference can be attributed to several combined effects:

- A smaller average grain size (~ 2.5 μm) increases the density of grain boundaries, enhancing scattering and intergranular tunnelling resistance.

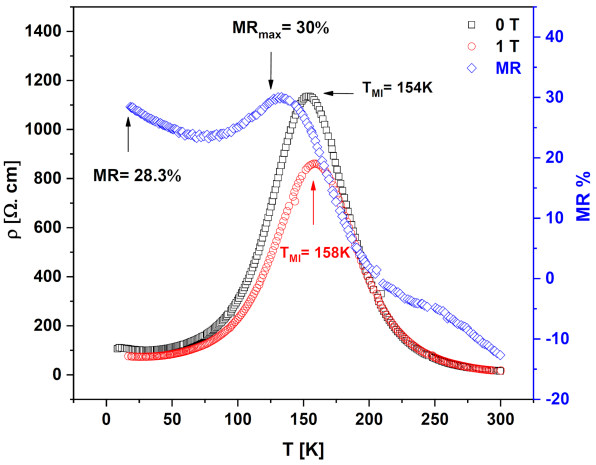

Fig. 9. Temperature dependence of resistivity (left axis) and magnetoresistance variation (right axis) for the $La_{0.7}Ca_{0.18}Ba_{0.12}Mn_{0.95}Sn_{0.05}O_3$ sample.

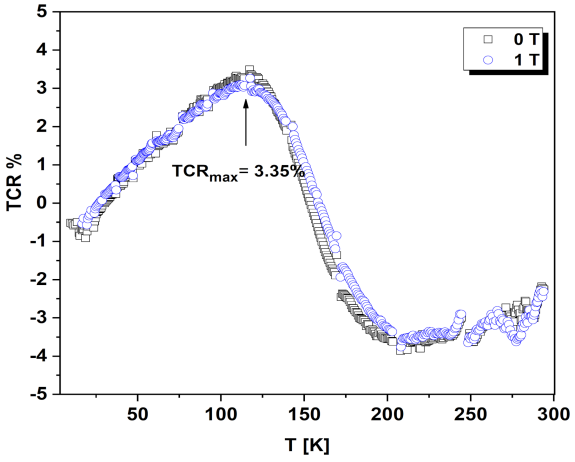

Fig. 10. Temperature coefficient of resistivity as a function of temperature for the $La_{0.7}Ca_{0.18}Ba_{0.12}Mn_{0.95}Sn_{0.05}O_3$ compound.

- A minor, insulating La_2O_3 secondary phase, identified by the Rietveld refinement, may be located along grain boundaries and act as additional barriers to charge transport.
- Variation in pellet density and porosity arising from differences in sintering temperature can likewise reduce the effective cross-sectional area available for current flow.

It is known that the application of an external magnetic field suppresses spin fluctuations, which results in a reduction in electrical resistivity. The compound sensitivity to an applied external magnetic field is described by magnetoresistance (MR), which is given by

$$\mathrm{MR} = \frac{\rho(0) - \rho(H)}{\rho(0)} \times 100\%, \tag{18}$$

where $\rho(H)$ and $\rho(0)$ are the resistivities at magnetic fields of 1 and 0 T, respectively. The MR vs T is shown in Fig. 9. For our sample, the plot shows that the magnetoresistance reached its maximum value ($\mathrm{MR_{max}}$) of $\simeq$ 30% around T_{MI}, which is the intrinsic magnetoresistance (IMR). This behavior has been associated with the double exchange mechanism [64]. On the other hand, the second value of MR at low temperature is the extrinsic magnetoresistance (EMR) and is caused by intergrain spin-polarized tunnelling (ISPT) through grain boundaries [65]. The EMR contribution tends to increase as the temperature decreases; its peak reached 28.3%.

The variation of the temperature coefficient of resistivity (TCR) of the LCBMSO sample versus temperature is depicted in Fig. 10. The coefficient TCR is mainly determined by ρ and the slope of the ρ–T curve. It is given by the following relation

$$\mathrm{TCR} = \left(\frac{1}{\rho}\,\frac{\mathrm{d}\rho}{\mathrm{d}T}\right) \times 100\%. \tag{19}$$

As shown in Fig. 10, the compound exhibits a maximum TCR value around T_{MI}, which reaches 3.35%. The TCR curve does not show a significant change when exposed to a 1 T external magnetic field. Its maximum value is higher compared to the values reported previously [47, 66]. The difference is mainly due to the sample synthesis conditions. Conversely, the maximum TCR value obtained in this work is inferior to the values reported in other studies.

In a previous study [68], it was found that doping significantly influenced the TCR value. In addition, several other factors may affect it, such as preparation method, sintering temperature, sample quality, tolerance factor (t), average A-site ionic radius $\langle r_{\mathrm{A}} \rangle$, and ceramic resistivity.

3.6. Conduction mechanism

To understand the different factors affecting the conduction mechanism in the compound, various theoretical models were applied to fit the $\rho(T)$ curves.

3.6.1. Low-temperature behavior ($T < T_{\mathrm{MI}}$)

In the low-temperature ferromagnetic regime ($T < T_{\mathrm{MI}}$), the transport mechanism in manganites typically depends on various scattering mechanisms, including those originating from grain or domain boundaries, electron–electron interactions and electron–magnon scattering. Resistivity data in this temperature range are analysed using the expression

$$\rho = \rho_0 - \rho_{0.5}\,T^{0.5} + \rho_2\,T^2 + \rho_5\,T^5, \tag{20}$$

where ρ_0 denotes the residual resistivity arising from domain and grain boundaries; $\rho_{0.5}\,T^{0.5}$ represents the weak localization, $\rho_2\,T^2$ refers to the

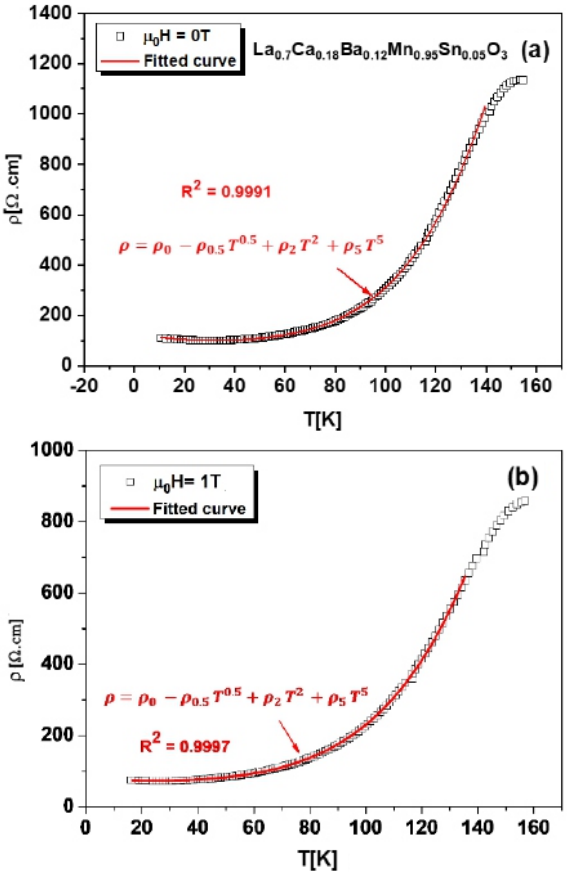

Fig. 11. Fitting curves for LCBMSO based on equation (20): (a) $\mu_0 H = 0$ T and (b) $\mu_0 H = 1$ T.

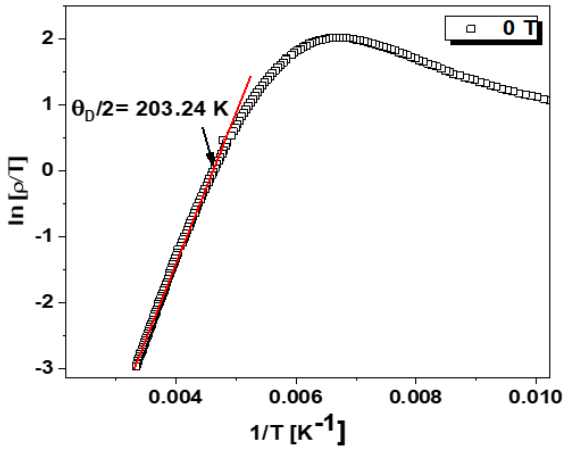

Fig. 12. Determination of the Debye temperature for the LCBMSO sample in a 0 T magnetic field.

electron–electron scattering process, whereas $\rho_5 T^5$ is attributed to electron–phonon scattering [69]. The results obtained from the curve fitting are provided in Table VII, and a representative plot is illustrated in Fig. 11.

A reduction in the fitting parameters is observed upon the application of a 1 T magnetic field. This behaviour can be explained by the decrease in spin

TABLE VII

Fitted parameters of the low temperatures resistivity data of $La_{0.7}Ca_{0.18}Ba_{0.12}Mn_{0.95}Sn_{0.05}O_3$.

Parameter	Unit	0 T	1 T
ρ_0	[Ω cm]	143.1928	91.3154
$\rho_{0.5}$	[Ω cm/K$^{0.5}$]	9.7140	4.6151
ρ_2	[Ω cm/K^2]	0.0120	0.0086
ρ_5 ($\times 10^{-8}$)	[Ω cm/K^5]	1.4471	0.9890
R^2		0.9991	0.9997

fluctuation caused by the application of an external magnetic field. Furthermore, it is worth noting that the residual resistivity ρ_0 is much larger than the other terms; this confirms the important role that grain boundaries play in the conduction process.

3.6.2. High-temperature behavior ($T > T_{MI}$)

In the high temperature regime, the conduction mechanism is commonly described using two different models, namely the variable range hopping (VRH) and small polaron hopping (SPH) models [70, 71]. The VRH model describes the electrical resistivity above T_{MI} and below $\theta_D/2$, where θ_D is the Debey temperature. The term $\theta_D/2$ refers to half of the Debye temperature and represents a characteristic temperature above which the phonon population becomes significantly activated. The SPH model is applied at temperatures exceeding $\theta_D/2$, as determined from the plot of $\ln(\rho/T)$ versus $(1/T)$ (see Fig. 12).

Firstly, the variable range hopping (VRH) model [72] is expressed as follows

$$\rho(T) = \rho_0 \left(\frac{T_0}{T}\right)^{1/4}, \tag{21}$$

where ρ_0 represents the resistivity coefficient, and T_0 is the characteristic temperature. It is related to the density of states near the Fermi level, $N(E_F)$, by

$$T_0 = \frac{24\,\alpha^3}{k_B N(E_F)}, \tag{22}$$

where $\alpha = 2.22$ nm^{-1} is the inverse of localization length, and k_B is Boltzmann's constant. The resistivity curves fitted using the VRH model are shown in Fig. 13. The fitting parameters T_0 and $N(E_F)$ are provided in Table VIII. It was noticed that when a magnetic field is applied, the value of T_0 decreases, whereas the value of $N(E_F)$ increases. This could be due to the decrease in resistivity; it is the evident impact of the increased charge carrier concentration at the Fermi level [73].

Secondly, the adiabatic small polaron hopping (ASPH) model [74] is given by the following expression

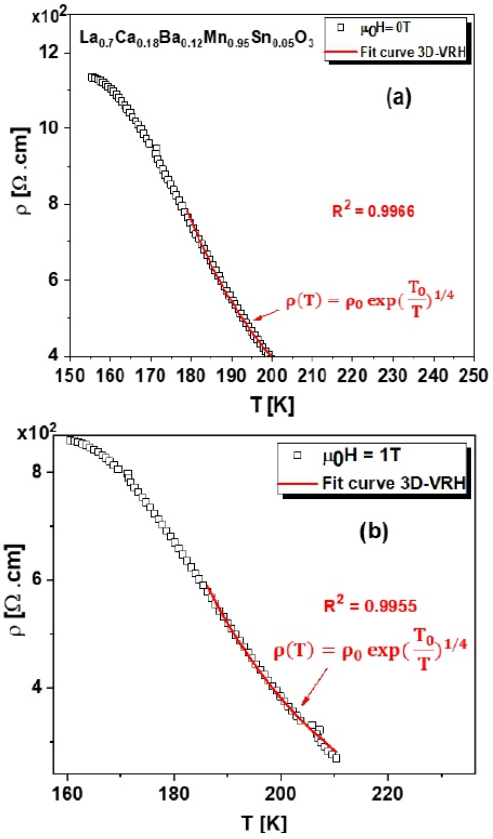

Fig. 13. Fitting curve of resistivity versus temperature obtained using the 3D-VRH model: (a) $\mu_0 H = 0$ T and (b) $\mu_0 H = 1$ T.

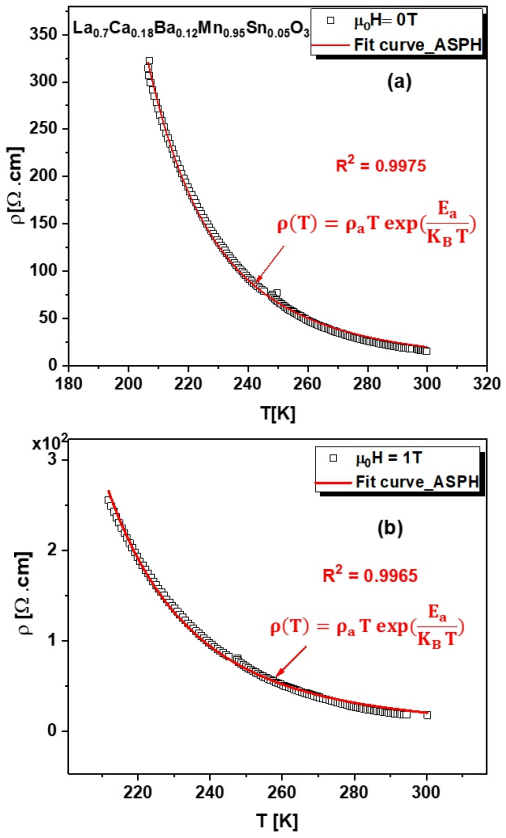

Fig. 14. Fitting curve of resistivity versus temperature obtained using the ASPH model: (a) $\mu_0 H = 0$ T and (b) $\mu_0 H = 1$ T.

TABLE VIII

Fitted parameters of the resistivity curves obtained using the 3D-VRH and ASPH models.

Parameter	Unit	0 T	1 T
Model (3D-VRH) $\rho(T) = \rho_0 \left(\frac{T_0}{T}\right)^{1/4}$			
ρ_0	[Ω cm]	1.217×10^{-8}	1.248×10^{-8}
T_0	[K]	6.867×10^{7}	6.793×10^{7}
$N(E_F)$	$\left[\frac{1}{\text{eV cm}^3}\right]$	1.417×10^{19}	1.432×10^{19}
R^2		0.9966	0.9955
Model (ASPH) $\rho(T) = \rho_a T \exp\left(\frac{E_a}{k_B T}\right)$			
$\theta_D/2$	[K]	203.24	205.65
ρ_a	[Ω cm]	6.078×10^{-5}	6.094×10^{-5}
T_0	[K]	2095.805	2103.646
E_a	[eV]	0.1815	0.1808
R^2		0.9975	0.9965

$$\rho(T) = \rho_a T \exp\left(\frac{E_a}{k_B T}\right), \tag{23}$$

where ρ_a is the residual resistivity, E_a is the activation energy for hopping conduction, and k_B represents the Boltzmann constant. Figure 14 displays the data fitted using (23) for the ASPH model. Table VIII indicates that when a magnetic field of 1 T is applied, the activation energy decreases, in agreement with the observed reduction in resistivity. Our value of E_a is in good agreement with previous studies [75, 76]. Both considered models provide satisfactory fits to our data in the semiconducting region. However, the ASPH model demonstrates a better correlation factor R^2 compared to the VRH model, which suggests that adiabatic small polaron hopping is the predominant transport mechanism.

4. Conclusions

In summary, a polycrystalline sample of $La_{0.7}Ca_{0.18}Ba_{0.12}Mn_{0.95}Sn_{0.05}O_3$ (LCBMSO) was successfully synthesized through a solid-state method. Rietveld refinement from XRD data revealed that LCBMCO crystallizes with orthorhombic symmetry with P*nma* space group. SEM micrograph showed the granular nature of the sample, with an average grain size of 2.53 μm. Moreover, magnetic measurements indicated that the manganite LCBMSO undergoes a magnetic transition from PM to FM at T_C, and the magnetic

susceptibility obeys the CW law. From the M–H curves at 1.8 and 100 K, it was observed that the LCBMSO sample exhibits ferromagnetic behavior, but at 300 K it shows paramagnetic behavior. Electrical investigations showed that the resistivity of LCBMSO has a metal–insulator transition at $T_{\mathrm{MI}} = 154$ K. The maximum magnetoresistance (MR) value of about 30% under $\mu_0 H = 1$ T was obtained. The temperature coefficient of resistivity (TCR) reached a value of 3.35%, suggesting that the sample is appropriate for bolometric applications. The resistivity data in the metallic region $T < T_{\mathrm{MI}}$ were fitted by the equation $\rho(T) = \rho_0 - \rho_{0.5} T^{0.5} + \rho_2 T^2 + \rho_5 T^5$. In the temperature range above T_{MI}, the resistivity $\rho(T)$ was fitted using the variable range hopping (VRH) model for temperatures above $\theta_{\mathrm{D}}/2$. However, below $\theta_{\mathrm{D}/2}$ the adiabatic small polaron hopping (ASPH) model was used to explain the resistivity behavior.

Acknowledgments

This work was supported by "The General Direction of Scientific Research and Technological Development — Algeria" (DGRSDT/MESRS).

References

[1] Y. Tokura, Y. Tomioka, *J. Magn. Magn. Mater.* **200**, 1 (1999).

[2] V.K. Pecharsky, K.A. Gschneidner, *Appl. Phys. Lett.* **70**, 3299 (1997).

[3] A.J. Millis, *Nature* **392**, 147 (1998).

[4] S. Zhao, X. Yue, X. Liu, *Ceram. Int.* **43**, 4594 (2017).

[5] R. Jha, S.K. Singh, A. Kumar, V.P.S. Awana, *J. Magn. Magn. Mater.* **324**, 2849 (2012).

[6] S.M. Yusuf, M. Sahana, K. Dörr, U.K. Rößler, K.-H. Müller, *Phys. Rev. B* **66**, 064414 (2002).

[7] G.H. Jonker, J.H. Van Santen, *Physica* **16**, 337 (1950).

[8] R. Li, L. Pi, Y. Zhang, *Solid State Commun.* **152**, 616 (2012).

[9] L.M. Rodriguez-Martinez, J.P. Attfield, *Phys. Rev. B* **58**, 2426 (1998).

[10] M.N. Iliev, M.V Abrashev, V.N. Popov, V.G. Hadjiev, *Phys. Rev. B* **67**, 212301 (2003).

[11] A. Urushibara, Y. Moritomo, T. Arima, A. Asamitsu, G. Kido, Y. Tokura, *Phys. Rev. B* **51**, 14103 (1995).

[12] P. Zhang, P. Lampen, T.L. Phan et al., *J. Magn. Magn. Mater.* **348**, 146 (2013).

[13] N. Sdiri, M. Bejar, E. Dhahri, *J. Magn. Magn. Mater.* **311**, 512 (2007).

[14] N. Kambhala, S. Angappane, *Phys. B Condens. Matter* **411**, 72 (2013).

[15] M. Khlifi, M. Bejar, E. Dhahri, P. Lachkar, E.K. Hlil, *J. Appl. Phys.* **111**, 103909 (2012).

[16] M.S. Islam, D.T. Hanh, F.A. Khan et al., *Phys. B Condens. Matter* **404**, 2495 (2009).

[17] D.T. Hanh, M.S. Islam, F.A. Khan, D.L. Minh, N. Chau, *J. Magn. Magn. Mater.* **310**, 2826 (2007).

[18] S.O. Manjunatha, A. Rao, T.-Y. Lin, C.-M. Chang, Y.-K. Kuo, *J. Alloys Compd.* **619**, 303 (2015).

[19] T.D. Thanh, T.H. Lee, T.L. Phan, D.A. Tuan, S.C. Yu, *J. Appl. Phys.* **115**, 17C706 (2014).

[20] R. Tripathi, V.P.S. Awana, N. Panwar et al., *J. Phys. D Appl. Phys.* **42**, 175002 (2009).

[21] M.-H. Phan, S.-B. Tian, S.-C. Yu, A.N. Ulyanov, *J. Magn. Magn. Mater.* **256**, 306 (2003).

[22] G.L. Reddy, Y.K. Lakshmi, S.M. Rao, P.V. Reddy, *J. Magn. Magn. Mater.* **362**, 20 (2014).

[23] S. Hcini, S. Zemni, A. Triki, H. Rahmouni, M. Boudard, *J. Alloys Compd.* **509**, 1394 (2011).

[24] I. Belal, F. Meriche, N. Mahamdioua et al., *Appl. Phys. A* **129**, 26 (2023).

[25] H. Qin, J. Hu, J. Chen, H. Niu, L. Zhu, *J. Magn. Magn. Mater.* **263**, 249 (2003).

[26] H. Song, W. Kim, S.-J. Kwon, J. Kang, *J. Appl. Phys.* **89**, 3398 (2001).

[27] J. Dhahri, S. Mnefgui, A. Ben Hassine, T. Tahri, M. Oumezzine, E.K. Hlil, *Phys. B Condens. Matter* **537**, 93 (2018).

[28] R.-W. Li, J.-R. Sun, Z.-H. Wang, S.-Y. Zhang, B.-G. Shen, *J. Phys. D Appl. Phys.* **33**, 1982 (2000).

[29] E. Tka, K. Cherif, J. Dhahri, *Appl. Phys. A* **116**, 1181 (2014).

[30] K. Chu, T. Sun, Y. Liu et al., *Ceram. Int.* **45**, 17073 (2019).

[31] X. Yu, H. Li, K. Chu, X. Pu, X. Gu, S. Jin, X. Guan, X. Liu, *Ceram. Int.* **47**, 13469 (2021).

[32] H.M. Rietveld, *J. Appl. Crystallogr.* **2**, 65 (1969).

[33] J. Rodríguez-Carvajal, "FullProf 2000: An Introduction to the Program", 2001, p. 132.

[34] F. Zheng, L.R. Pederson, *J. Electrochem. Soc.* **146**, 2810 (1999).

[35] K. Momma, F. Izumi, *J. Appl. Crystallogr.* **44**, 1272 (2011).

[36] D. Kumar, N.K. Verma, C.B. Singh, A.K. Singh, *AIP Conf. Proc.* **2009**, 020013 (2018).

[37] H. Agarwal, J.A. Alonso, Á. Muñoz, R.J. Choudhary, O.N. Srivastava, M.A. Shaz, *J. Alloys Compd.* **845**, 156355 (2020).

[38] P.G. Radaelli, G. Iannone, M. Marezio et al., *Phys. Rev. B* **56**, 8265 (1997).

[39] Y. Regaieg, G. Delaizir, F. Herbst et al., *Mater. Lett.* **80**, 195 (2012).

[40] W. Xia, K. Leng, Q. Tang, L. Yang, Y.Xie, Z. Wu, X. Zhu, *AIP Adv.* **11**, 35007 (2021).

[41] U. Holzwarth, N. Gibson, *Nat. Nanotechnol.* **6**, 534 (2011).

[42] K. Siraj, M. Khaleeq-ur-Rahman, S.I. Hussain, M.S. Rafique, S. Anjum, *J. Alloys Compd.* **509**, 6756 (2011).

[43] K. Ravichandran, G. Muruganantham, B. Sakthivel, *Phys. B Condens. Matter* **404**, 4299 (2009).

[44] G. K. Williamson, W.H. Hall, *Acta Metall.* **1**, 22 (1953).

[45] A. Dhahri, M. Jemmali, E. Dhahri, M.A. Valente, *J. Alloys. Compd.* **638**, 221 (2015).

[46] C.T. Rueden, J. Schindelin, M.C. Hiner, B.E. DeZonia, A.E. Walter, E.T. Arena, K.W. Eliceiri, *BMC Bioinform.* **18**, 526 (2017).

[47] S. Boufligha, N. Mahamdioua, F. Denbri, F. Meriche, S.P. Altintas, C. Terzioglu, *J. Low Temp. Phys.* **206**, 232 (2022).

[48] J. Ye, C. Bu, Z. Han, G. He, J. Li, Y. Chen, *Mater. Lett.* **171**, 55 (2016).

[49] G.V.S. Rao, C.N.R. Rao, J.R. Ferraro, *Appl. Spectrosc.* **24**, 436 (1970).

[50] I.S. Debbebi, H. Omrani, W. Cheikhrouhou-Koubaa, A. Cheikhrouhou, *J. Phys. Chem. Solids* **113**, 67 (2018).

[51] V.S. Kolat, H. Gencer, M. Gunes, S. Atalay, *Mater. Sci. Eng. B* **140**, 212 (2007).

[52] J.T. Burke, *J. Chem. Educ.* **74**, 1213 (1997).

[53] R.A. El-Mallawany, *Infrared Phys.* **29**, 781 (1989).

[54] M.-H. Phan, S.-B. Tian, S.-C. Yu, A.N. Ulyanov, *J. Magn. Magn. Mater.* **256**, 306 (2003).

[55] M. Dhahri, A. Zaidi, K. Cherif, J. Dhahri, E.K. Hlil, *J. Alloys Compd.* **691**, 578 (2017).

[56] M. Bourguiba, M.A. Gdaiem, M. Chafra, E.K. Hlil, H. Belmabrouk, A. Bajahzar, *Appl. Phys. A* **125**, 375 (2019).

[57] G.G. Lonzarich, L. Taillefer, *J. Phys. C Solid State Phys.* **18**, 4339 (1985).

[58] E. Bouzaiene, A.H. Dhahri, J. Dhahri, E.K. Hlil, A. Bajahzar, *J. Magn. Magn. Mater* **491**, 165540 (2019).

[59] C. Kittel, *Introduction to Solid State Physics*, 6th ed., Trans. Y. Uno, N. Tsuya, A. Morita, J. Yamashita, Maruzen, Tokyo 1986, p. 124.

[60] M.R. Laouyenne, M. Baazaoui, S. Mahjoub, W. Cheikhrouhou-Koubaa, M. Oumezzine, *J. Alloys Compd.* **720**, 212 (2017).

[61] S. Mahjoub, M. Baazaoui, R. M'nassri, H. Rahmouni, N.C. Boudjada, M. Oumezzine, *J. Alloys Compd.* **608**, 191 (2014).

[62] K. El Maalam, M.B. Ali, H. El Moissaoui et al., *J. Alloys Compd.* **622**, 761 (2015).

[63] C. Zener, *Phys. Rev.* **82**, 403 (1951).

[64] G. Venkataiah, V. Prasad, P.V. Reddy, *J. Alloys Compd.* **429**, 1 (2007).

[65] G. Channagoudra, A.K. Saw, V. Dayal, *Emergent Mater.* **3**, 45 (2020).

[66] S. Vadnala, T.D. Rao, P. Pal, S. Asthana, *Phys. B Condens. Matter* **448**, 277 (2014).

[67] A. Pal, B.S. Nagaraja, K.J. Rachana, K.V. Supriya, D. Kekuda, A. Rao, C.R. Li, Y.K. Kuo, *Mater. Res. Express* **7**, 036102 (2020).

[68] J. Jiang, S. Zhao, T. Sun, Q. Chen, X. Liu, *Ceram. Int.* **44**, 3915 (2018).

[69] D. Varshney, D. Choudhary, M.W. Shaikh, E. Khan, *Eur. Phys. J. B* **76**, 327 (2010).

[70] S.O. Manjunatha, A. Rao, V.P.S. Awana, G.S. Okram, *J. Magn. Magn. Mater.* **394**, 130 (2015).

[71] D. Li, Q. Chen, Z. Li, Y. Li, H. Zhang, Y. Zhang, *Ceram. Int.* **44**, 3448 (2018).

[72] G. Yellaiah, M. Nagabhushanam, *J. Cryst. Growth* **421**, 33 (2015).

[73] S. Mollah, H.L. Huang, H.D. Yang, S. Pal, S. Taran, B.K. Chaudhuri, *J. Magn. Magn. Mater.* **284**, 383 (2004).

[74] A.S. Alexandrov, B.Y. Yavidov, *Phys. Rev. B* **69**, 073101 (2004).

[75] Z. Mohamed, A.B. Hassen, A. Somrani, E.K. Hlil, *J. Low Temp. Phys.* **209**, 198 (2022).

[76] V.P. Kumar, *Acta Phys. Pol. A* **147**, 383 (2025).